Materials & Design 254 (2025) 114057

Contents lists available at ScienceDirect

Materials & Design

journal homepage: www.elsevier.com/locate/matdes

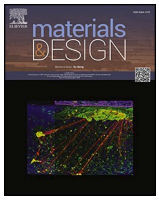

Metrological evaluation and classification of porosity in metal additive manufacturing using X-ray computed tomography

Ibon Holgado [a,*], Naiara Ortega [b], José A. Yagüe-Fabra [c], Soraya Plaza [b], Herminso Villarraga-Gómez [d]

[a] Aeronautics Advanced Manufacturing Center, CFAA (UPV/EHU), Bizkaia Technology Park, Building 202, Zamudio 48170, Spain
[b] Faculty of Engineering of Bilbao, UPV/EHU, Plaza Torres Quevedo 1, Bilbao 48013, Spain
[c] I3A, University of Zaragoza, María de Luna 3, 50018 Zaragoza, Spain
[d] Carl Zeiss Industrial Quality Solutions, LLC, Wixom, MI, USA

ARTICLE INFO

Keywords:
Additive manufacturing
X-ray computed tomography
Measurement uncertainty
Porosity characterization
Porosity classification

ABSTRACT

Ensuring the structural integrity of metal additive manufacturing (AM) components is challenging due to inherent porosity, which critically affects mechanical performance. The impact of porosity depends on its morphology, determined by the formation mechanism, making it a core focus for characterization and classification through advanced non-destructive testing methods. This study introduces a novel X-ray computed tomography (XCT) based methodology for the metrological assessment of porosity in laser powder bed fusion manufactured AlSi10Mg components. A new modular artefact, specifically designed to contain real porosity, enables the application of the substitution method for porosity characterization, including the assignment of measurement uncertainty, representing a novel application for evaluating real porosity morphology using XCT. Advanced porosity analysis algorithms, including 'VGDefX', 'OnlyThreshold', and 'VGEasyPore', are benchmarked to determine the one yielding the lowest dimensional measurement uncertainty across varying material thicknesses. The VGDefX algorithm, which incorporates a probability-based and iterative approach, demonstrates superior repeatability, achieving subvoxel systematic errors and measurement uncertainties for dimensions exceeding five times the voxel size. Based on the pore characterization results, a classification methodology using the most discriminating porosity parameters is developed. Leveraging volumetric mean gray value, this method distinguishes over-melting from under-melting porosity in a real component with >95 % accuracy.

1. Introduction

Additive Manufacturing (AM) offers significant design flexibility, enabling the production of metal parts with complex geometries that are often unachievable by conventional manufacturing routes. This capability facilitates lightweight structures and improved functional integration, contributing to enhanced operational efficiency [1]. Among the metals employed in AM, aluminum alloy AlSi10Mg is one of the most prevalent for advanced structural applications due to its high mechanical strength, excellent corrosion resistance, superior thermal conductivity, and favorable weldability [2]. Despite significant progress in this field, the widespread adoption of AM parts faces challenges, primarily due to production-related issues such as defect formation and the lack of standardized quality control protocols [3]. International organizations, including NASA and the Aerospace Technology Institute (ATI), have highlighted significant technological gaps that hinder the reliable adoption of AM in critical applications, emphasizing the need for advanced non-destructive testing (NDT) techniques tailored to the complexities of AM [4,5].

The formation of porosity is common in aluminum alloys manufactured by laser powder bed fusion (PBF-LB), where the material's high reflectivity and thermal conductivity require elevated laser energy, frequently resulting in unstable melt pools and an increased risk of defect formation [6]. As a result, over-melting conditions increase the likelihood of keyhole-type pores due to excessive energy input, forming gas-filled cavities from localized metal vaporization [7]. Over-melting pores (OMP) generally exhibit smooth, rounded shapes [8]. Conversely, under-melting conditions, caused by insufficient laser

* Corresponding author.
E-mail address: ibon.holgado@ehu.eus (I. Holgado).

https://doi.org/10.1016/j.matdes.2025.114057
Received 17 December 2024; Received in revised form 28 March 2025; Accepted 5 May 2025
Available online 6 May 2025

power or excessive hatch spacing, lead to lack-of-fusion pores. Undermelting pores (UMP) are generally characterized by sharp edges and poorly bonded boundaries due to incomplete melting and consolidation [7]. A more detailed classification of defect types in PBF-LB processes can be found in ISO/ASTM TR 52905:2023 [9].

Previous studies have demonstrated that the specific type of porosity present, critically impact mechanical properties, including fatigue life and structural integrity. Moreover, it is widely acknowledged that localized pore characteristics, rather than volumetric porosity alone, are critical for defining more precise acceptance criteria in AM components [10–12].

To address the pressing need for standardized evaluation of AM components, the recent ISO/ASTM TR 52905:2023 outlines NDT methods specifically tailored to the unique requirements of AM processes and their complex 3D geometries. The standard emphasizes that, amongst NDT techniques, X-ray computed tomography (XCT) is the most effective method for dimensional metrology and internal feature assessment in AM parts [9].

XCT is a useful NDT technique for quantification and characterization of porosity, which uses X-rays to capture a series of radiographs of an object in a single revolution or just over half, followed by a reconstruction algorithm that generates a volumetric digital representation, enabling detailed analysis of both internal and external structures [13–15]. XCT-based dimensional measurements offer valuable insights for AM process optimization and part conformity assessment. However, reliable interpretation of results requires addressing measurement uncertainty, which remains a focus of ongoing research due to the complexity of factors influencing the scanning process [16]. Addressing metrological traceability gaps is essential for ensuring reliable XCT-based porosity analysis in AM.

1.1. Metrological evaluation methods for XCT porosity measurement uncertainty

The quantification of uncertainty of XCT porosity measurements is a fundamental metrological challenge due to the absence of well-accepted models of the entire measurement process and consequently the lack of internationally standardized procedures [17]. The ISO 15530 series, originally developed for coordinate metrology systems (CMSs), describes four main methods for uncertainty evaluation of dimensions, with recent efforts adapting these methods to XCT measurements [18].

Approaches based on the Guide to the Expression of Uncertainty in Measurement (GUM) primarily focus on individual error sources within the XCT process rather than encompassing the entire measurement scenario. While several studies have identified major contributors, such as digital detector sensitivity [19], surface determination algorithms [20] and noise effects [21], comprehensive GUM-based evaluations for XCT porosity measurements remain underexplored. This limitation arises from the complexity of addressing the numerous error sources inherent to the XCT process. Fig. 1 illustrates the substantial impact of porosity analysis algorithm choices on segmented pore geometries, demonstrating how different surface determination algorithms can significantly affect XCT porosity measurements.

Simulation-based approaches, as outlined in ISO 15530-4, employ virtual measurement tools to estimate task-specific uncertainty [22]. These simulations provide valuable insights into XCT processes but face limitations in fully accounting for the complex interactions of X-rays with material structures since random errors and repeatability effects are often oversimplified or equated with noise [23,24]. Recent reviews emphasize the necessity of incorporating methods that explicitly account for these random errors [18]. Currently, simulation-based approaches for XCT porosity measurements remain insufficiently validated and incomplete for widespread application [25].

The multiple measurement strategies method, initially developed for tactile CMSs, has also been explored for XCT uncertainty evaluation. Although this approach involves repeated measurements under varying conditions to assess repeatability, its application to porosity analysis is constrained by practical challenges such as reorienting and repositioning parts within the XCT system. Furthermore, Zanini et al. highlights that uncertainty determined via this method may be overestimated compared to alternative empirical approaches and does not inherently account for scale errors in XCT systems, requiring additional tests with calibrated standards [26].

The substitution method, outlined in the VDI/VDE 2630–2.1 guidelines, which adapts ISO 15530–3 for tactile CMMs to XCT, has emerged as one of the most practical approaches for XCT uncertainty quantification [27,28]. This method does not require an explicit evaluation of measurement uncertainty for individual influence of error source but requires calibrated artefacts as reference objects, enabling the XCT to act as a comparator. Differences between measured values and the calibrated dimensions of the artefact are used to estimate measurement uncertainty. Although some attempts have been made to apply this method to XCT porosity measurements [29], this method was never applied before for AM generated real pores morphology evaluation due

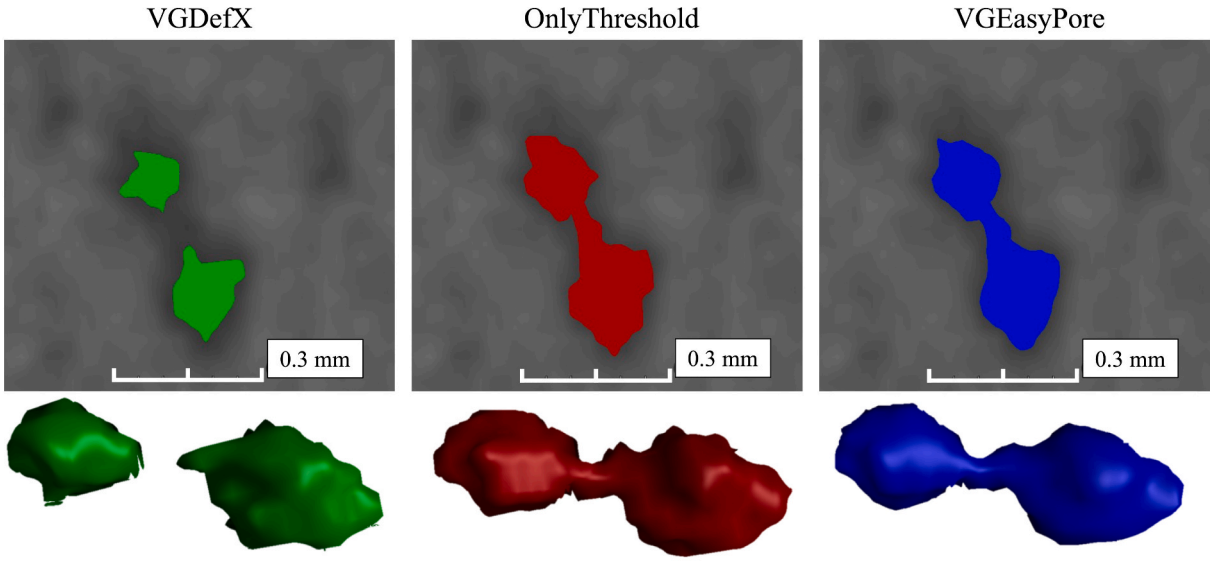

Fig. 1. Impact of porosity analysis algorithm choice on the segmentation of the same pore (voxel size: 44 μm): comparison of 2D and 3D segmented geometries obtained using three different XCT thresholding methods: VGDefX, OnlyThreshold, and VGEasyPore.

to the difficulty of performing calibration measurements (on which the method bases its implementation) on real pores non-accessible from the outside. This gap in research limits the broader application of previous efforts beyond academic/scientific settings.

Fig. 2 presents an overview of existing artefacts made of different materials, designed for XCT-based internal feature assessments [9,23,29–32]. While these artefacts include a range of geometries, such as artificial porosity and CAD-seeded internal flaws, they often fail to replicate the complex physics and variability of pore morphologies formed during AM processes.

Regarding aluminum artefacts, Hermanek et al. [29] and Chahid et al. [32] proposed aluminum alloy artefacts with regular-shaped hemispherical artificial cavities to study porosity-like flaws in controlled environments. However, beyond these efforts, no significant advancements have been made toward establishing traceability in porosity measurements, as highlighted by recent reviews [18,33], which concluded that XCT-based porosity measurement remains an open question, requiring further metrology-focused research.

Staude et al. [31] introduced an aluminum artefact containing porosity, scanned at an improved spatial resolution and signal-to-noise ratio as a reference. However, the absence of uncertainty assessments significantly undermines the traceability of these measurements. Improved resolution alone is insufficient to establish reference values without corresponding uncertainty evaluations.

In order to address the limitations identified in current XCT porosity traceable measurement approaches, this study proposes a novel modular artefact specifically designed to contain real over-melting porosity, which enables the implementation of the substitution method for porosity characterization, including the assignment of measurement uncertainty. The paper also examines the influence of cumulative material thickness embedding the pores. The presented approach, to the best of our knowledge, has not been previously applied for evaluating real porosity morphology using XCT. This work extends beyond the current literature data, which predominantly addresses NDT detection capabilities using artefacts with CAD-seeded internal flaws, surface-accessible defects, or idealized geometries. By evaluating physically generated flaws with unique morphologies formed during the PBF-LB process, this study addresses a key technological gap and contributes to the refinement of NDT acceptance criteria for AM parts.

Furthermore, the porosity characterization results derived from the artefact are applied to a real AM test object made from the same material and featuring a comparable thickness range. Based on the artefact's pore characterization results, a classification methodology is developed using the most discriminating porosity parameters, including compactness, sphericity, mean gray value, and projected area (%) along the primary cylinder's axis. Experimental results demonstrate that incorporating volumetric mean gray value significantly enhances defect classification, achieving over 95 % accuracy in distinguishing between over-melting and under-melting defects, thereby addressing a critical challenge in AM quality control.

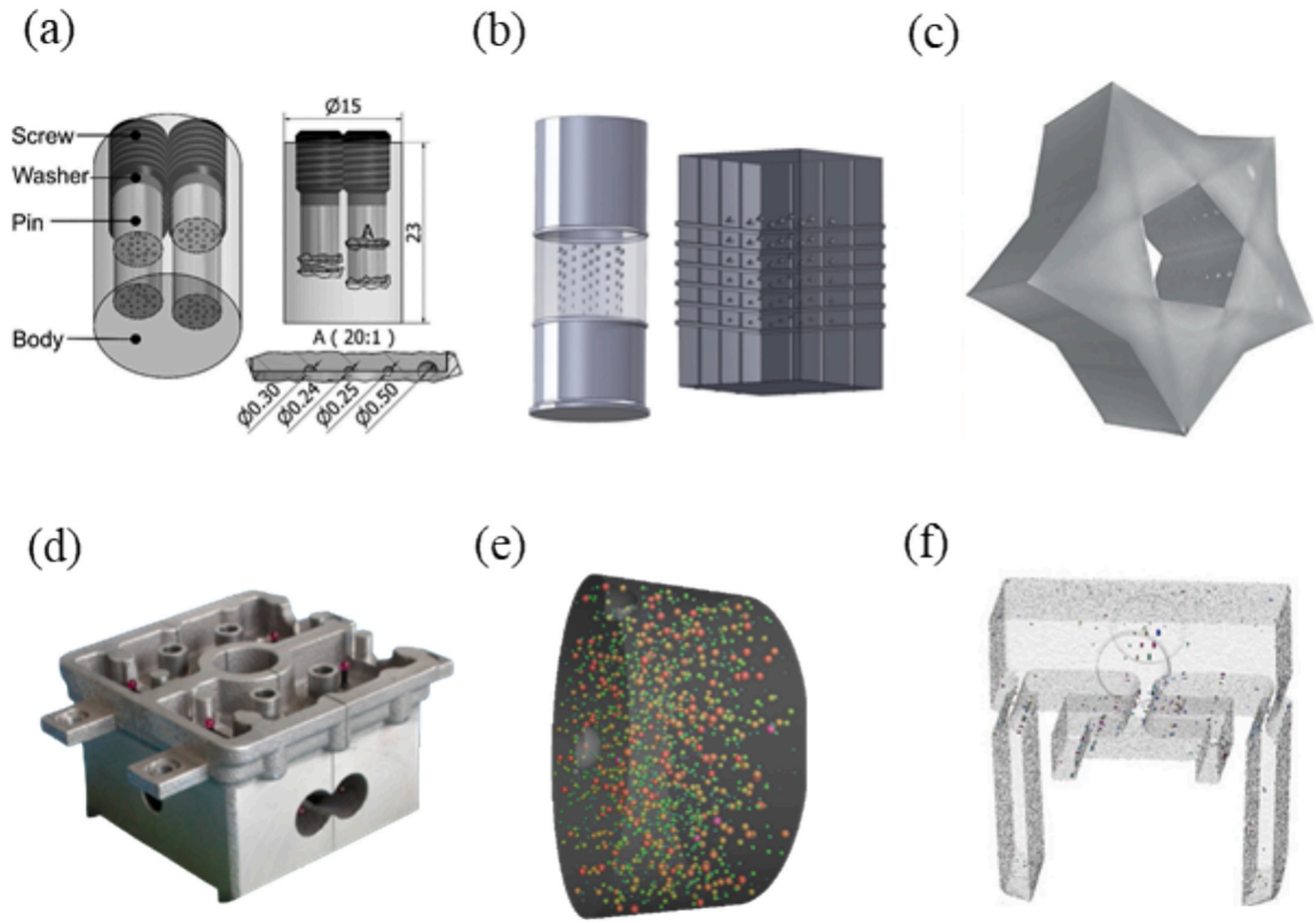

Fig. 2. Overview of artefacts designed for internal features assessments and calibration using XCT. (a) Artefact with artificial porosity [29], (b) Artificial defect reference objects [30], (c) Star artefact [9] (d) Mini-Cylinder Head No.5 [31], (e) Digital porosity twin [23] and (f) AlSi10Mg artefact [32].

2. Materials and methods

2.1. Material measure description

The material measure was specifically designed for XCT-based porosity characterization and to assess the impact of cumulative thickness on XCT measurement accuracy. This artefact, referred to as the "Modular Volumetric Artefact" is a volumetric assembly that features an internal AM-generated plate with high porosity, designed to be disassembled for calibration using a traceable measurement system that requires direct access to the features being measured. Each component of the Modular Volumetric Artefact was fabricated from aluminum alloy (AlSi10Mg).

The design includes semi-circumferential adjustments linking two monolithic half-cylinders of 60 mm length. A 3 mm thick AM plate of 130 mm length containing porosity induced by over-melting during the PBF-LB process is embedded in the cylinders. Two modular Assembled Modular Volumetric artefacts (hereafter referred to as material measures) were manufactured, differing only in cylinder diameter. The geometry and dimensions of the artefacts are illustrated in Fig. 3.

The primary cylinders were precision-machined using a 5-axis Yasda YBM950V machining center, while the 3 mm thick AM plates were produced by PBF-LB process. Then, the AM plates were finished using wire electrical discharge machining (WEDM) with an ONA AX3 system to accurately shape and fit them to the primary cylinders. WEDM was selected due to its non-contact thermal erosion mechanism, which avoids plastic deformation and burr formation that could obstruct or alter pore geometry, issues typically associated with conventional mechanical cutting methods. To verify that the WEDM process did not interfere with accurate pore evaluation, a metallographic analysis was conducted on an AlSi10Mg specimen sectioned under identical machining parameters. The resulting recast (white) layer was consistently below 8 μm, more than an order of magnitude smaller than the evaluated pore diameters, confirming its negligible impact on dimensional measurements.

The PBF-LB process was performed on a Renishaw AM500 machine equipped with a 500 W Ytterbium fiber laser and using powder with a particle size distribution of 20–63 μm. During production, the plates were positioned vertically, with the largest dimension aligned with the build direction. After the manufacturing process, the AM plates were subjected to a stress-relieving heat treatment of 1.5 h at 180 °C.

To induce OMPs, the PBF-LB parameters were adjusted to increase laser energy density, leading to fluid dynamic instabilities that trapped ambient and metal-contained gases, resulting in pore formation [34]. The energy density (E) was calculated using the following Eq. (1):

$$E = \frac{P}{V \bullet H \bullet t} \quad (1)$$

where P is the laser power (W), V is the scanning speed (mm/s), H is the hatch distance (mm), and t is the layer thickness (mm).

A preliminary study was carried out using 50 mm × 10 mm × 3 mm coupons to identify the optimal conditions for generating high porosity density. Five parameter sets were evaluated by varying the scanning speed (1.25 m/s to 0.8 m/s) and hatch spacing (0.15 mm to 0.10 mm), while maintaining a constant laser power of 500 W (maximum machine capacity) and a layer thickness of 60 μm. The highest evaluated energy density (104.16 J/mm3), approximately 40 % higher than the manufacturer's recommended settings, resulted in the greatest pore concentration and was selected for fabricating the material measure AM plates.

To ensure the material measure stability and enable XCT scale factor correction (voxel size adjustment) before XCT dimensional measurements, the design incorporates eight precision-engineered (grade 5) Al_2O_3 spheres, each with a 4 mm nominal diameter and minimal form error (3 μm), which is considered negligible in terms of its influence on the scale factor correction calculation. These spheres were accommodated using an industrial cyanoacrylate adhesive, ensuring structural stability within the design limits of the artefacts (adhesion strength of 0.03 ± 0.01 Mpa [35]). Prior to fixating the spheres, specific positions and pre-defined depths for the sphere-embedding holes were milled using a ball nose mill cutter. The milling depth was configured to achieve a protrusion exceeding 50 % of the sphere's diameter, resulting in approximately 44 % of the total sphere surface being accessible for probing using a 1 mm diameter stylus.

2.2. Material measure calibration

An initial high-resolution XCT scan with a 5 μm voxel size was conducted on a localized 7.5 mm × 6 mm × 6 mm region of the AM plates in the Ø30 mm thick material measure to estimate the pore size distribution. The probability-based and iterative thresholding method ('VGDefX' algorithm) was applied for post-processing this high-resolution scan. The results indicated that the majority of pores had diameters within the 0.2–0.3 mm range. Based on this analysis, ten OMPs within this dominant size range, comprising thousands of

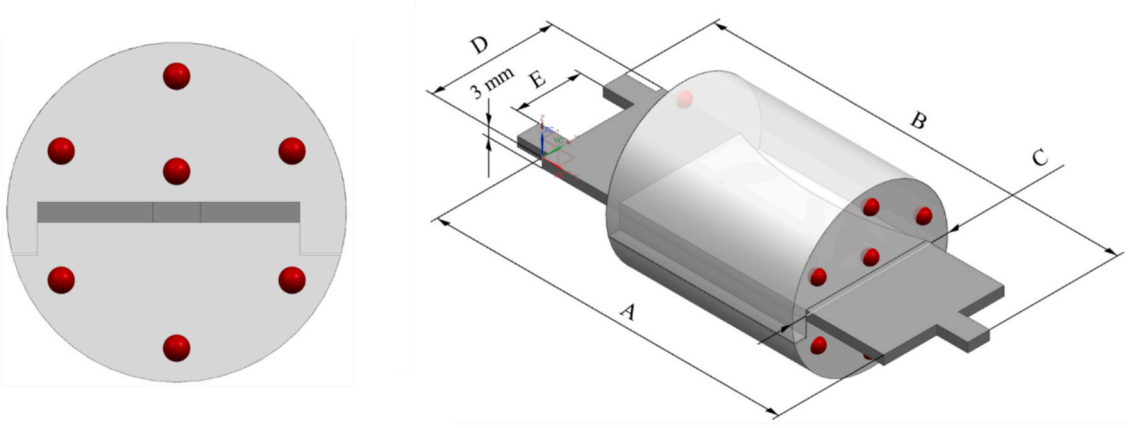

	A	B	C	D	E
Ø30 mm artefact	110 mm	130 mm	Ø30 mm	22.45 mm	4.45 mm
Ø50 mm artefact	110 mm	130 mm	Ø50 mm	38.65 mm	20.65 mm

Fig. 3. Design of the Assembled Modular Volumetric Ø30 mm and Ø50 mm artefacts. 3D and lateral views with general dimensions.

detected pores (approximately 350 pores per mm3), were randomly selected from the surface of Plane A on both the Ø30 mm and Ø50 mm material measures.

The selection of these ten OMPs started with the establishment of the Coordinate System (CS), ensuring a consistent and systematic approach across both the traceable optical instrument measurements (Fig. 4b), used for calibrating pore diameter and circularity measurements, and the XCT measurements (Fig. 4a). Plane A was first determined using the least squares method based on the area of the AM plate extending from the main cylinders, employing a point density of 10,000 points. The Z-direction was defined as perpendicular to this plane. The dimensions and positioning of the planes are illustrated in Fig. 4.

The calibration of the ten selected pores was conducted by measuring both the diameter and circularity using the ZEISS O-Inspect multi-sensor measuring machine by an accredited calibration laboratory. Measurements were performed using the least squares method, chosen for its robustness in identifying the average geometric center and minimizing sensitivity to local deviations. In addition, the X, Y, and Z coordinates of each OMP center were recorded to ensure further accurate pore localization in the XCT data. The results from the calibration are presented in Table 1. The calibration measurement expanded uncertainty (U_{cal}) remained consistently at 0.005 mm across the selected pores, representing a relative uncertainty range from 1.68 % to 2.45 % of the measured pore sizes.

The calibration expanded uncertainty was calculated by multiplying the standard measurement uncertainty by a coverage factor of k = 2, yielding a confidence level of approximately 95 % for a normal distribution. The standard uncertainty was evaluated according to the certified guidelines in EA-4/02M:2022 [36].

The calibration of the distances between the centers of the Al_2O_3 spheres (used for scale factor correction) was conducted using a ZEISS F-25 multi-sensor coordinate measuring machine (CMM) with a maximum permissible error (MPE) of (0.25 + L/666) μm, where L is the measured length in mm. The measurements were performed using a 1 mm diameter probe with a 12 mm stem length. Least square fitting was used for sphere centers from the measured surface points. The expanded uncertainty for all measured distances was 0.005 mm (k = 2). The sphere distances are presented in Table 2, which includes a minimum of five distinct unidirectional measurements across various spatial orientations.

The scale factors were determined through the relation between the calibrated reference measurements and those measured using XCT. This process was replicated in five repeat scans performed with identical scan parameters. The standard deviation of the scale factor across these five repeated measurements, multiplied by a safety factor of 1.4 [37], was assigned as the standard uncertainty attributed to the scale factor correction. The maximum uncertainty obtained was 0.04 μm, confirming that no additional uncertainty associated with voxel size correction was required. This also justifies the assumption that the minimal form error (3 μm) of the high-precision spheres has a negligible effect on the scaling factor accuracy.

As observed in the XCT cross-sectional images in Fig. 5, the gap between the monolithic cylinders and the AM plate with porosity is imperceptible, reflecting the high precision and optimal fit between the assembled components.

2.3. Test object description

The substitution method requires a test object that closely matches the calibrated artefact in terms of cumulative thickness, material, dimensions, and geometry. To meet these requirements, a test object inspired by an auxiliary aircraft engine nozzle, an industrially relevant component currently produced using AM, was fabricated using the Renishaw AM500 PBF-LB machine.

As shown in Fig. 6, the test object contains two distinct regions (slices) with diameters of 30 mm and 50 mm (highlighted in Fig. 6a), corresponding to the same cumulative thicknesses used in the material measures. Within each region, sections with different characteristics can be found (illustrated in Fig. 6c). The first section has 3 mm in height and includes OMPs while the second section has 1 mm in height and is free of defects. The last section has 3 mm in height and includes under-melting UMP defects. The OMP defects were created by replicating the same over-melting conditions used in the material measure, while the UMP defects were induced by reducing the PBF-LB recommended energy density by 20 %. Specifically, the power was set to 400 W, scanning speed to 2 m/s, hatch distance to 0.19 mm, and layer height to 0.06 mm.

2.4. XCT measurement uncertainty assessment using the substitution method

To estimate the measurement systematic error and uncertainty, the substitution method was applied, following guidelines adapted from VDI/VDE 2630–2.1 (adapted to XCT from the ISO 15530–3 for tactile

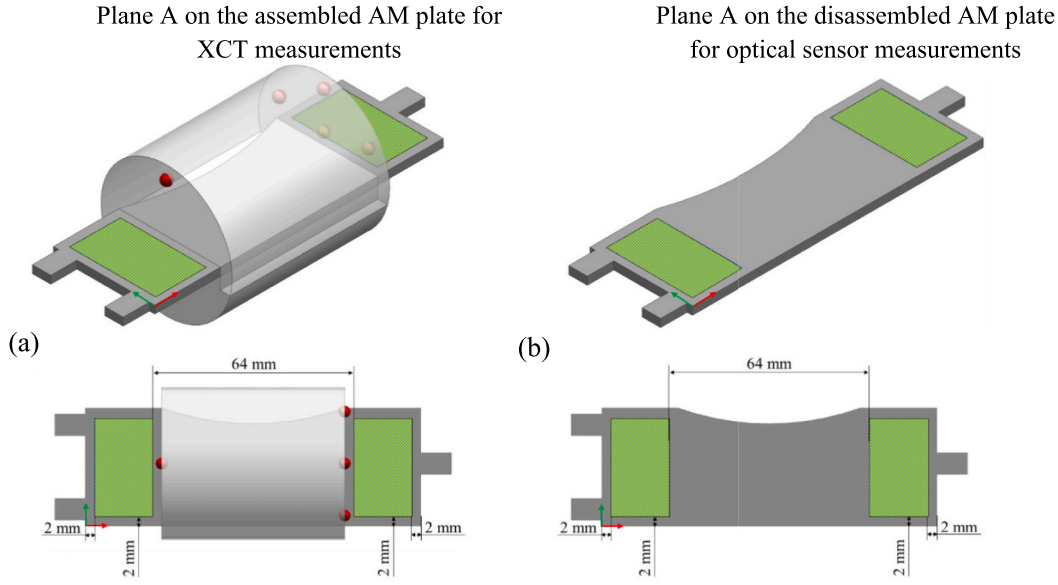

Fig. 4. Systematic criterion for establishing the reference Plane A and general dimensions of the AM plate. (a) Reference Plane A established on the assembled AM plate for XCT measurements, and (b) Reference Plane A established on the disassembled AM plate for optical sensor measurements.

Table 1
Diameter and circularity results from the ZEISS O-Inspect optical sensor for the ten selected pores. All values in millimeters (mm).

Ø30 mm thick material measure										
Pore N°	1a	2a	3a	4a	5a	6a	7a	8a	9a	10a
Diameter	0.248	0.228	0.212	0.236	0.238	0.297	0.246	0.244	0.242	0.267
Circularity	0.013	0.015	0.011	0.012	0.012	0.011	0,014	0.012	0.022	0.019
U_{cal}	0.005	0.005	0.005	0.005	0.005	0.005	0.005	0.005	0.005	0.005
Ø50 mm thick material measure										
Pore N°	1b	2b	3b	4b	5b	6b	7b	8b	9b	10b
Diameter	0.248	0.225	0.227	0.230	0.254	0.271	0.258	0.204	0.240	0.230
Circularity	0.009	0.009	0.007	0.013	0.012	0.013	0.010	0.010	0.018	0.013
U_{cal}	0.005	0.005	0.005	0.005	0.005	0.005	0.005	0.005	0.005	0.005

Table 2
Distances between centers of the spheres employed for scale factor correction in the material measures. All values are in millimeters (mm).

Distance	Ø30 mm	Ø50 mm
C1-C3	5.996	14.016
C1-C2	8.538	17.392
C4-C3	8.592	20.227
C2-C4	16.019	34.044
C1-C5	60.913	62.238

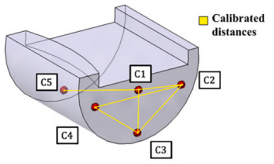

CMMs) [28]. The substitution method requires a reference artefact (material measure in this case), calibrated with sufficiently low uncertainty that meets similarity conditions to the test object. The material measure needs to be scanned repeatedly to correct systematic errors (denoted as b) and to determine the measurement uncertainty (U_{MP}). The U_{MP} is described by Eq. (2):

$$U_{MP} = k \cdot \sqrt{u_{cal}^2 + u_{drift}^2 + u_p^2 + u_w^2 + u_b^2} \quad (2)$$

where k represents a coverage factor with a 95 % confidence level. The term u_{cal} represents the standard uncertainty associated with the calibrated optical sensor reference measurements ($u_{cal} = \frac{U_{cal}}{k_{cal}}$). For the test object, u_{cal} is derived from the material measure's measurement uncertainty (U_{MP}). The u_{drift} accounts for potential variations in the shape of the material measure since calibration. However, in this case, it was neglected because the XCT scans were conducted immediately after the optical sensor measurements. The u_p represents the standard uncertainty of the repeated measurements. While ISO 15530–3 recommends twenty repeated measurements for tactile CMMs, this was adjusted to five repeated measurements due to the time and cost constraints of XCT. To account for the reduced number of repetitions, a safety factor of 1.4 was applied, ensuring a 95 % confidence level [37]. The term u_w accounts for potential differences between the material measure and the test object, such as differences in thermal expansion or pore's manufacture variability, that is, difference in similarity. For the material measure, u_w contribution was neglected, as both the optical sensor and XCT measurements were performed on the same pores, ensuring direct comparability with no differences in similarity. For the test object, u_w reflects potential differences size, and geometry between the material measure and the test object, which must meet similarity conditions for adequate application of the substitution method. The pore manufacturing variability assessment, presented in Table 4 of Section 3.2, justifies the assumption of sufficient similarity. In line with established practices in similar studies [37], potential variability (u_w) was incorporated into the repeatability uncertainty (u_p) through repeated measurements of individual pores in the test object. This approach prevents overestimating expanded uncertainty by addressing variability within u_p rather than treating u_w as a separate term.

The last term, u_b, represents the uncertainty associated with the correction of the systematic error (b), calculated with the differences between the calibrated values and the mean measured values obtained via XCT ($u_b = \Delta t \bullet u_{ab} \bullet l$). The calculation of the u_b component was based on the premise that it should include at least the standard uncertainty u_{ab} linked with the linear coefficient of thermal expansion of the calibrated material and the temperature variation during the measurement process from its reference of 20 °C [38], which is the standard temperature reference used for dimensional measurements. For this study, the uncertainty of the CTE is derived from variations between 23.8 and 23.9 μm/m·°C. The temperature gradient during the measurement process was minimal, with variations confined to ±0.4 °C from the reference 20 °C. Given the small magnitude of the features being measured and the minimal temperature gradient, the resulting u_b value was very small and contributed negligibly to the overall expanded uncertainty. Correcting for systematic error involves subtracting the bias (b) from the measured values and the corrected measurement result, Y_{MP}, is then calculated using Eq. (3):

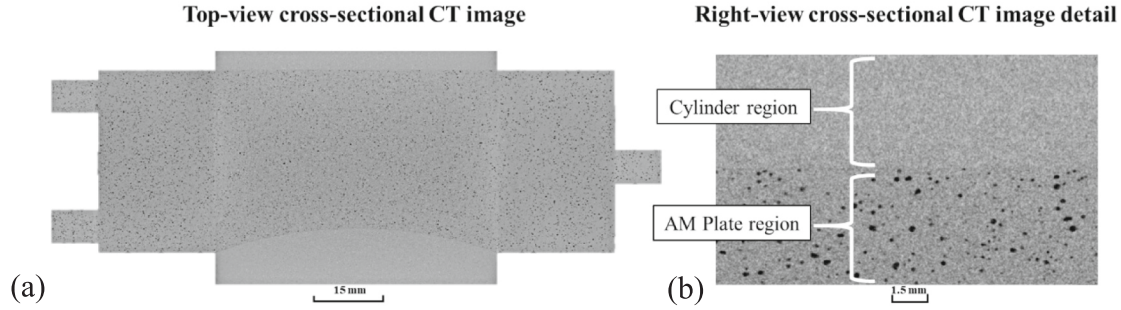

Fig. 5. XCT image displaying regions of both a fully dense cylinder and an AM plate (containing porosity) of the material measure. (a) Top-view XCT cross-sectional image and (b) right-view XCT cross-sectional image.

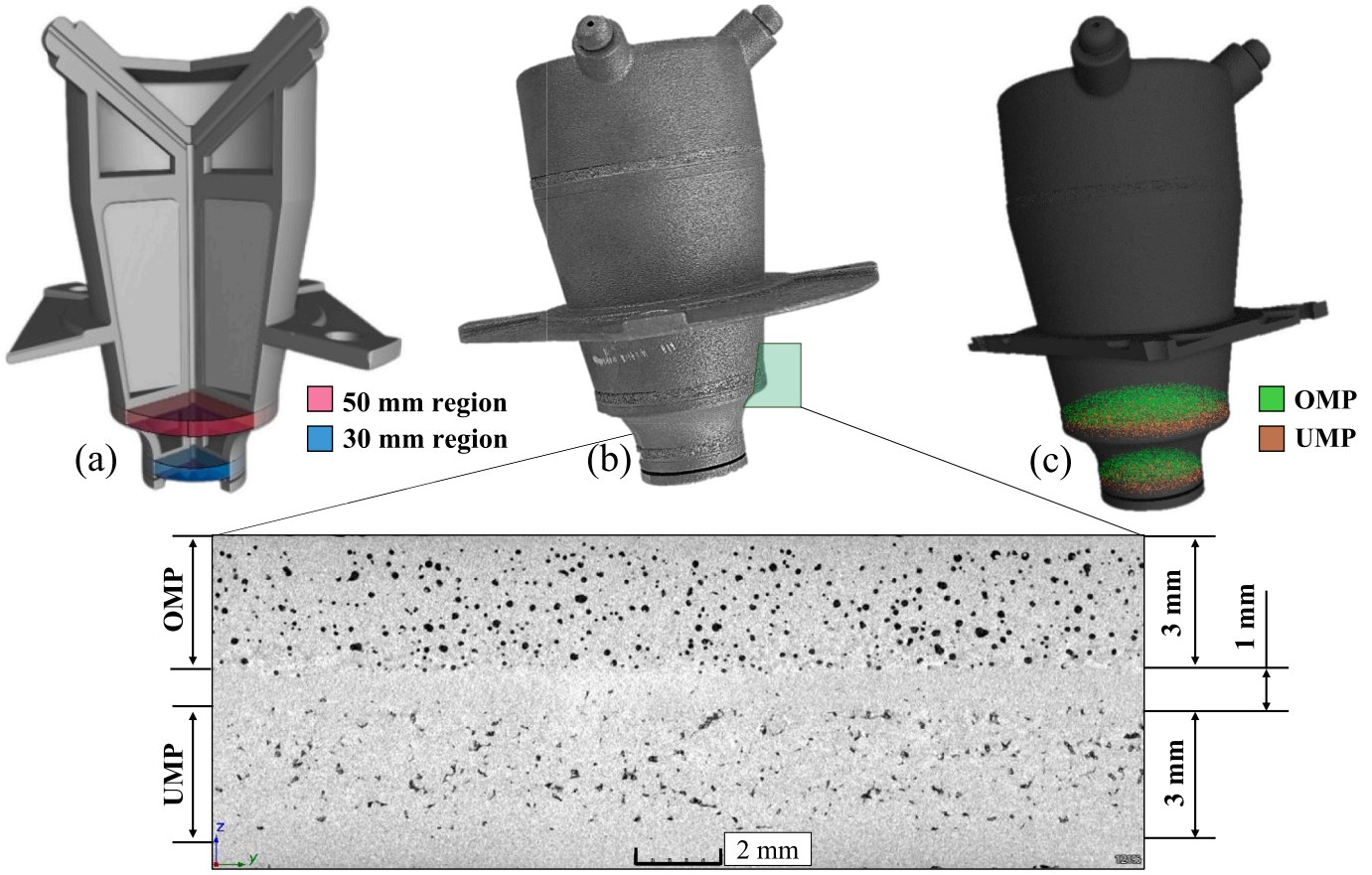

Fig. 6. Test object description. (a) Clipped virtual part highlighting distinct thickness-evaluated regions, (b) Cross-sectional perspective showcasing layers generated by distinct PBF-LB parameters in the actual object and (c) XCT scan presenting porosity analysis within 30 mm and 50 mm diameter regions of the test object.

$$Y_{MP} = y_{MP} - b \pm U_{MP} \quad (3)$$

where y_{MP} refers to the uncorrected XCT measurement of the test object features.

2.5. XCT porosity characterization and classification procedure

The material measures (Ø30 mm and Ø50 mm cumulative thickness) and the test object were scanned using a ZEISS Metrotom 1500 XCT system equipped with a 225 kV/500 W high-power microfocus X-ray source. The system's maximum permissible error (MPE) specifications of the XCT systems were tested in accordance with VDI/VDE 2617-13 and VDI/VDE 2630–1.3, as verified by calibration certificate no. 8581628904-10. The system's MPE for sphere distance measurements was specified as MPE SD (TS) = (4.5 + L/50) μm, where L represents the measurement length in mm.

Following the substitution method to ensure metrological traceability in XCT porosity measurements, each sample underwent five sequential scans under controlled environmental temperature conditions. The same data post-processing procedure was applied to the XCT measurements and to those obtained from the traceable optical sensor. Fig. 7 illustrates the general workflow of the applied procedure.

The XCT system includes a digital DXR detector with a resolution of 3072 × 3072 pixels. The voltage was set at 175 kV, while the tube current was increased to reduce exposure time, at 324 μA. The exposure time for each projection was set at 2000 ms. These parameters were chosen for both the material measure and test object, and remained constant throughout testing, ensuring consistency in data collection. To reduce beam hardening effects and remove low-energy photons from the X-ray beam, a 1 mm copper filter was used. The material measures underwent scanning in an upright orientation but slightly tilted (1°–4°) to minimize Feldkamp artifacts.

The rotary table's position was adjusted to achieve maximum magnification for both material measures and test object, allowing full volume projection onto the detector. This setup resulted in an isotropic voxel size of 44 μm. With this voxel size, the majority of the OMP diameters (ranging between 0.2 mm and 0.3 mm) in the material measure were represented by at least four voxels, thus enabling accurate pore detection [39,40]. After capturing 2200 radiographs during the scanning, these were used to create a 3D volume with a XCT reconstruction software (Metrotom OS, Carl Zeiss Industrielle Messtechnik GmbH). The reconstructed XCT data were subjected to quantitative analysis employing the porosity analysis module within VGStudio MAX 3.4 software.

Porosity characterization was performed by measuring pore diameter and circularity through a sequential post-processing of the XCT data. Pores were detected and segmented using three VGStudio algorithms: 'VGDefX', 'OnlyThreshold', and 'VGEasyPore'. The 'VGDefX' algorithm initiates segmentation by identifying seed voxels with a high probability of belonging to pores and iteratively expands the region based on probabilistic criteria until a predefined condition or the maximum allowable contrast difference is reached. This method enables accurate detection of complex pore geometries, although it is computationally more demanding due to its iterative nature. The 'OnlyThreshold' algorithm applies a global threshold for pore detection based on grayscale intensity, making it computationally efficient and best suited for high-contrast, low-noise materials. The 'VGEasyPore' algorithm uses a local grayscale histogram to determine a local threshold. Subvoxel accuracy is achieved by adapting the boundary placement based on the grayscale values of neighboring voxels [41].

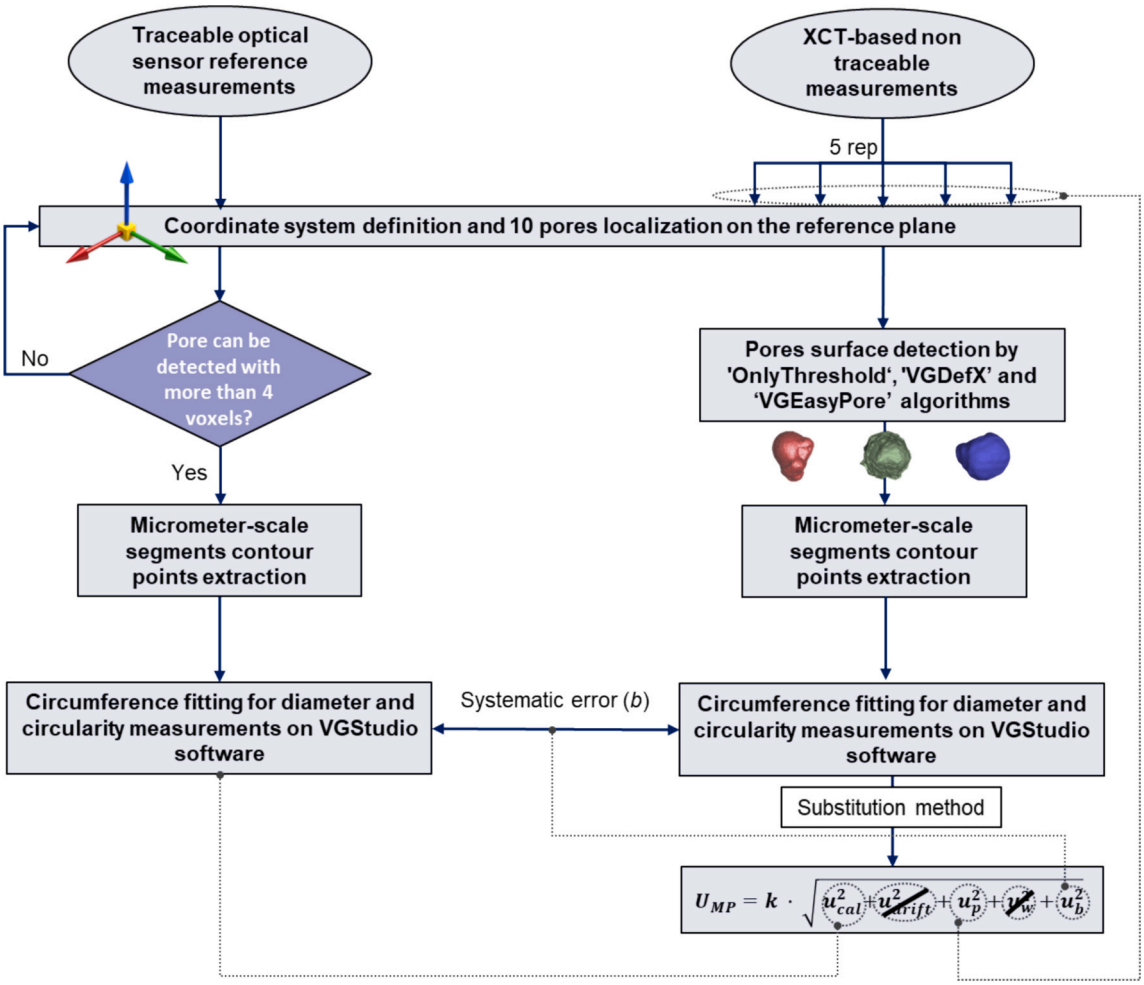

Fig. 7. Systematic workflow for XCT-based porosity characterization in the material measure.

The porosity analysis algorithms were applied using the default parameter settings recommended by the software. These parameters could be adjusted for specific porosity inspection cases, provided that consistency is maintained by applying the same parameters in both the material measure used for metrological characterization and the test object. After applying each thresholding method, the contour profile of each segmented pore was extracted from the cross-section corresponding to the reference plane (Plane A, shown in Fig. 4) and discretized into micrometer-scale segments. These contour profiles were then fitted to circumferences using the least squares method in VGStudio software to determine pore diameters. Circularity was also calculated based on same least squares fitting approach. Each pore's contour extraction was repeated five times, using the five independent XCT scans for each material measure, to assess measurement repeatability under identical scanning conditions. The same measurement data post processing procedure was applied to the measurements obtained from the traceable optical sensor, which were then compared to the XCT results.

In addition to diameter and circularity, several volumetric properties, such as compactness, sphericity, mean gray value, and projected area along the primary cylinder's axis were assessed.

These properties were then used to further classify defects into OMP and UMP categories in the test object, differentiating between pores caused by over-melting or under-melting during the PBF-LB process.

3. Results and discussion

This section provides a comprehensive analysis of the localized porosity measurements from both the material measure and the test object. Section 3.1 presents the evaluation of XCT-based measurements, focusing on systematic errors in diameter and circularity, which were determined using three distinct pore surface detection algorithms. Additionally, the key contributors to measurement uncertainty are analyzed, and the expanded uncertainty is calculated for each set of measurements. Furthermore, Section 3.1 includes a complementary high-resolution XCT analysis (5 μm voxel size) to preliminarily assess the methodology's applicability to small gas-entrapped pores, typically found under optimized PBF-LB conditions. Section 3.2 focuses on the classification of porosity resulting from over-melting and under-melting in the test object, extending the traceable link from the diameter and circularity measurements of the pores' material measure.

3.1. Evaluation of porosity analysis algorithms

This section presents the results of diameter and circularity mea-

surements obtained for the ten selected pores in the Ø30 mm and Ø50 mm material measures, using the aforementioned XCT data post-processing algorithms in the 44 μm voxel size scans. Appendix A provides the detailed measurements (y_{MP}), obtained by each algorithm, along with the systematic error (b), the expanded measurement uncertainty (U_{MP}) and a breakdown of the contributing sources of uncertainty.

The data in Appendix A reveal that, regardless of pore diameter or the cumulative thickness in which the pores are embedded, the calibration uncertainty component (u_{cal}), derived from the optical sensor, contributes less than 14 % of the total expanded measurement uncertainty (U_{MP}) in the worst-case scenario. The primary source of uncertainty appears to be the uncertainty of the repeated measurements (u_p). Additionally, the uncertainty associated with the correction of systematic error (u_b) is negligible relative to both u_p and u_{cal}. Since the XCT scans were conducted under stable environmental conditions ($\Delta t \approx 0$ °C), and the measured features are small ($l \approx 0$), the resulting u_b approaches zero. For this reason, this contributor has been omitted from the Appendix Tables.

Fig. 8 illustrates the XCT results for average pore diameter and circularity for the ten selected pores in the 30 mm and 50 mm thick material measures, as analyzed by each porosity detection algorithm (VGDefX, OnlyThreshold, and VGEasyPore). The expanded measurement uncertainty U_{MP} ($k = 2$) is indicated by the error bars for each measurement set. Notably, for the VGEasyPore results, pore number 1a was not detected in any of the repeated scans. For pores 4a, 1b, and 3b, the pore was not detected in at least one out of the five repeated XCT scans, which significantly increased the U_{MP} for diameter measurements and resulted in larger error bars.

The general results in Fig. 8 indicates that, overall, the VGDefX algorithm, yields the most consistent measurements with lower uncertainty. It minimizes the mean uncertainty across all measurements and provides U_{MP} values for both diameter and circularity measurements that are generally smaller than the voxel size used in the scans. In contrast, the OnlyThreshold algorithm, while often comparable to VGDefX, exhibits discrepancies in some cases (e.g., pore number 3b), where a single pore was misidentified as two adjacent pores in at least one measurement repetition. This discrepancy was not observed in VGDefX segmentations. Regarding the VGEasyPore results, the large error bars in some cases are primarily due to the algorithm failing to detect the pore in one or more repeated scans, leading to a significant increase in U_{MP}.

The superior performance of the VGDefX algorithm is attributed to its probability-based detection method, which effectively identifies voxels that are likely to belong to the pore. This method refines the segmentation through multiple iterations. These iterations tend to converge on similar voxel selections across repeated measurements, thereby improving both detection accuracy and repeatability. In contrast, VGEasyPore and OnlyThreshold rely on single-step detection methods. This reliance makes them more sensitive to small variations in grayscale caused by image noise or artifacts. As a result these algorithms often exhibit less consistent pore boundary detection across repeated scans.

To complement the main analysis performed at 44 μm voxel size and to preliminarily validate the applicability of the proposed XCT-based methodology, the initial high-resolution scan at 5 μm voxel size described in Section 2.2 was reanalyzed, also using five repeated XCT scans. This 5 μm voxel size scan, conducted on the 30 mm thick material measure, was originally employed to estimate pore size distribution but also satisfies the requirement of detecting pores below 0.050 mm in diameter with at least four voxels. Pores within this size range represent typical small gas-entrapped porosity, which is inherent to the PBF-LB process even under optimized manufacturing parameters. Ten randomly selected pores with diameters below 0.050 mm were processed using the same porosity algorithms and workflow applied in the main 44 μm voxel size analysis. The results, presented in Fig. 9, confirmed the same trends observed in the primary study, with VGDefX providing the highest repeatability and the lowest U_{MP}, generally below the voxel size, while VGEasyPore exhibited the poorest performance, even lower than in the 44 μm voxel size scans. As these smaller pores were not calibrated in this study, the same u_{cal} value used for the larger, calibrated pores was applied to estimate U_{MP} in this complementary assessment. While this approach may underestimate the expanded uncertainty, the results remain consistent with the trends observed in the main analysis.

Despite being presented solely as a complementary validation, the results shown in Fig. 9 reinforce the broader applicability of the

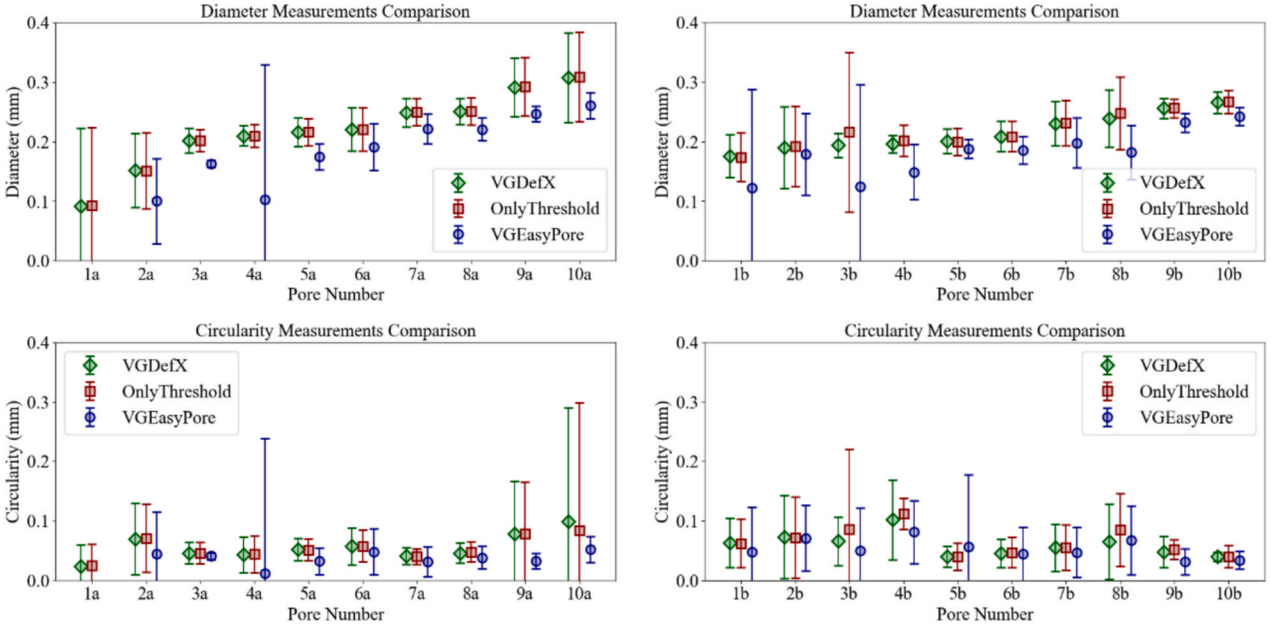

Fig. 8. XCT-measured pore diameters and circularity after detection with VGDefX, OnlyThreshold, and VGEasyPore algorithms for the 30 mm thick material measure (left) and for the 50 mm thick material measure (right).

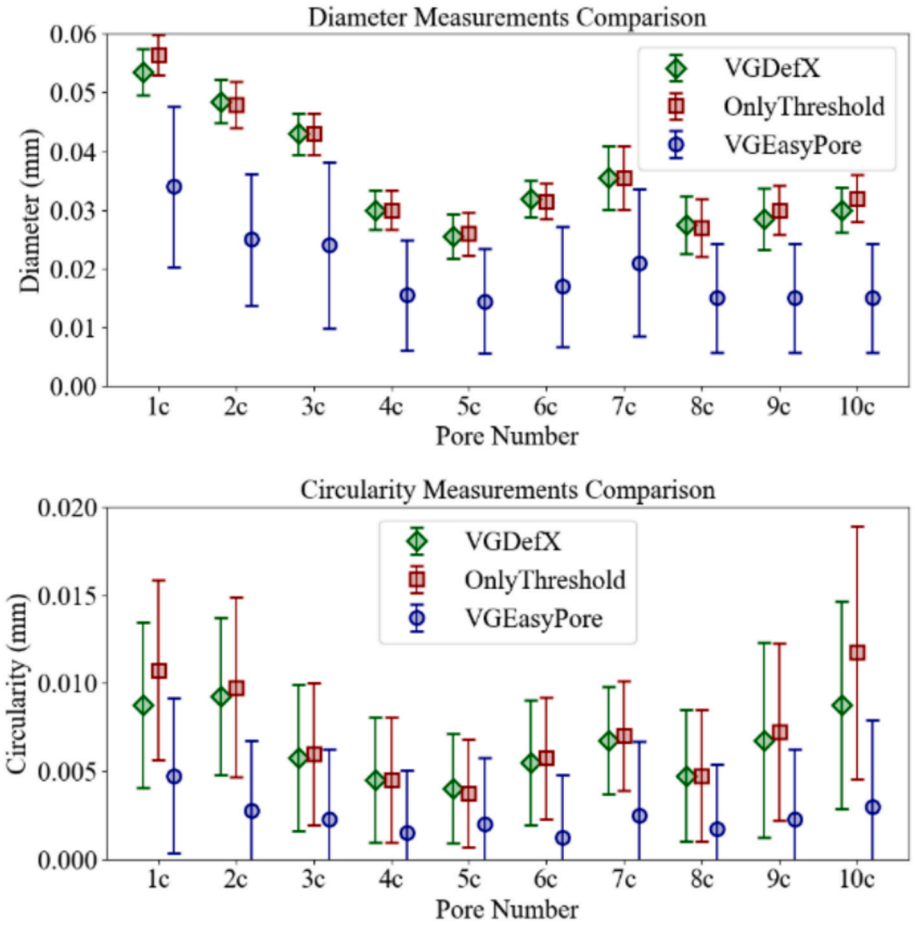

Fig. 9. XCT-measured pore diameters and circularity after detection with VGDefX, OnlyThreshold, and VGEasyPore algorithms for the 30 mm thick material measure using the initial high-resolution 5 µm voxel size scan.

Table 3
Mean U_{MP} for the diameter and circularity of the ten selected pores using the three porosity analysis algorithms, evaluated in the Ø30 mm and Ø50 mm thick material measures. All values are in millimeters (mm).

Measurand	Diameter			Circularity		
Algorithm	VGDefX	OnlyThreshold	VGEasyPore	VGDefX	OnlyThreshold	VGEasyPore
Mean U_{MP} (Ø30 mm thick material measure)	0.046	0.046	0.049	0.050	0.052	0.049
Mean U_{MP} (Ø50 mm thick material measure)	0.030	0.046	0.061	0.040	0.045	0.056

proposed XCT-based methodology to the typical diameter range of gas-entrapped pores. Hereafter, all subsequent results refer exclusively to the 44 µm voxel size scans.

To further quantify the robustness of each porosity algorithm under different imaging conditions, Table 3 summarizes the mean U_{MP} for both diameter and circularity across the ten pores in the 30 mm and 50 mm thick material measures, segmented using the three porosity analysis algorithms.

The results indicate that VGEasyPore, which determines pore boundaries via subvoxel grayscale interpolation, is more affected by the image degradation caused by the increased cumulative thickness. This image degradation is attributed to beam hardening effects, which reduce local contrast and introduce greater gray value variability between repeated measurements, leading to increased U_{MP} values at higher thickness. In contrast, VGDefX and OnlyThreshold operate at the voxel level during detection and perform interpolation only after segmentation, making them less affected grayscale distortions caused by beam hardening. Notably, the VGDefX algorithm, which incorporates a probability-based and iterative approach, demonstrates improved measurement repeatability as thickness increases, suggesting enhanced robustness in reduced image quality conditions.

Following the evaluation of measurement uncertainty for each porosity algorithm dataset, the accuracy of the two measured parameters, diameter and circularity, was assessed by calculating the bias between calibrated optical sensor values and the mean values from repeated XCT measurements. The resulting diameter measurement bias for the ten selected pores across the two material measure thicknesses is depicted in Fig. 10.

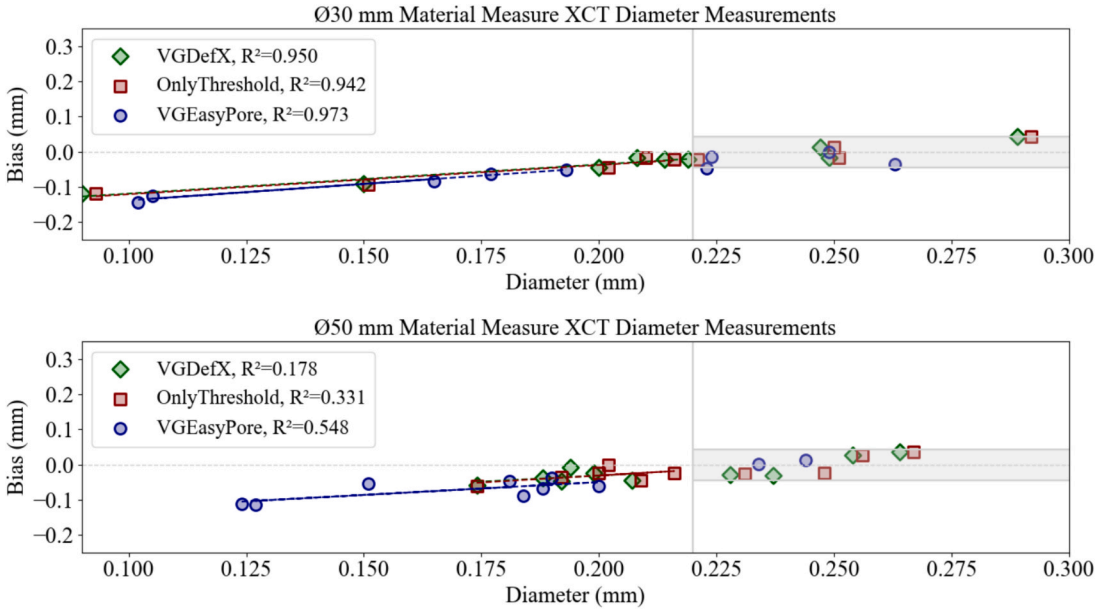

Fig. 10. Bias in XCT-measured pore diameters of material measures. Dots represent the measured bias relative to the calibrated optical sensor value. The shaded gray band represents the voxel size used in the XCT scans (0.044 mm), and the vertical gray line indicates the point where the pore diameter equals five times the voxel size (0.220 mm).

As illustrated in Fig. 10, once the pore diameter measurement exceeds five times the voxel size (vertical gray line), all evaluated algorithms demonstrate consistent measurements with a stabilized systematic error near the voxel size length. This trend is evidenced by all measured bias values falling within the shaded gray area, which represents the voxel size. For cumulative thickness of 30 mm, the systematic error remains proportional to the measured diameter below this threshold (i.e., 0.220 mm, calculated as 0.044 mm × 5), showing a linear relationship with an R^2 greater than 0.94 across all algorithms. Furthermore, within the 30 mm thickness, bias measurements for certain pores, particularly using the VGDefX and OnlyThreshold algorithms, display stabilized systematic error even below the five-voxel threshold. In contrast, the 50 mm thickness measurements show greater variability in systematic error, rendering the regression less robust.

Fig. 11 illustrates the bias observed in circularity measurements for the same ten preselected pores of the material measures, using the three porosity analysis algorithms.

Fig. 11 shows a consistent bias pattern in circularity measurements across all three algorithms, with the bias exhibiting a near-linear relationship to the magnitude of the measured circularity. Additionally, there is a trend of increasing variability in repeated measurements as circularity increases. The enhanced repeatability observed for measurements with smaller circularity values, as presented in the tables of Appendix A, can likely be attributed to the voxelization process in a continuous medium. Features with dimensions smaller than the voxel size are typically approximated by the voxel structure, leading to a smoother pore contour representation and contributing to repeatable

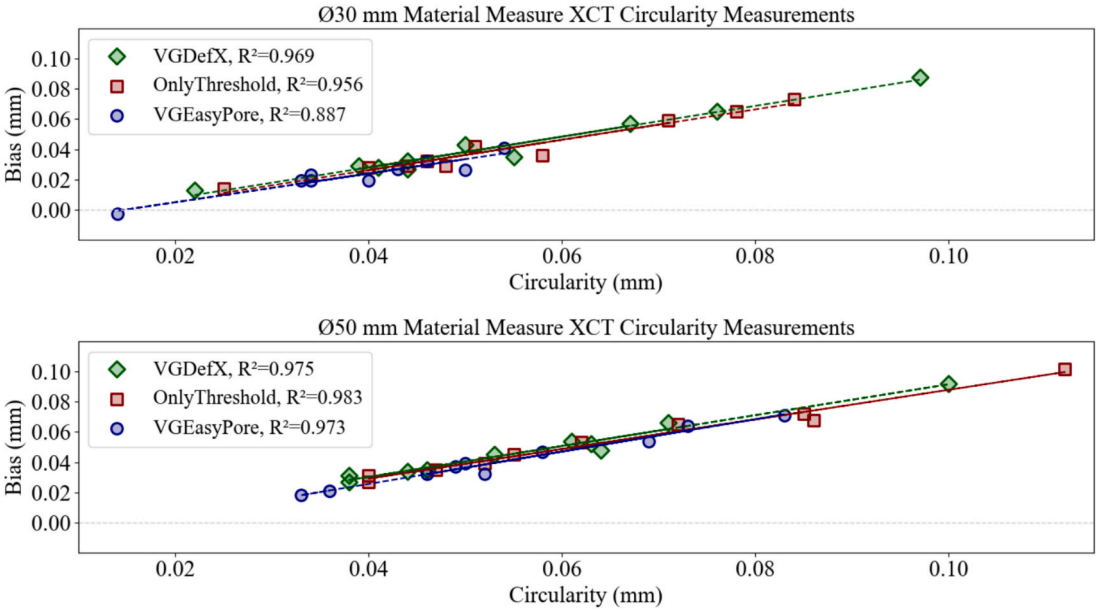

Fig. 11. Bias in XCT-measured pore circularity of the material measures. Dots represent the measured bias relative to the calibrated optical sensor value.

measurements with reduced expanded uncertainty (U_{MP}).

Unlike diameter measurements, changes in cumulative thickness do not significantly affect the bias in circularity measurements.

3.2. Over and under-melting porosity classification criteria

Building on the porosity characterization results presented in Section 3.1, twenty OMPs and twenty UMPs, randomly selected from 30 mm and 50 mm cumulative thickness 3 mm-high slices in the test object were measured by XCT. To ensure methodological consistency, the random selection was constrained to pores within the predefined size range of 0.2–0.3 mm, in accordance with the porosity characterization performed on the material measure. The probability-based and iterative thresholding method ('VGDefX') was used exclusively for pore surface detection in this analysis, as it yielded the lowest measurement uncertainties in diameter and circularity.

The expanded measurement uncertainty for the test object measurements was calculated using Eq. (2). The u_{cal} component was calculated as the mean U_{MP} from VGDefX repeated measurements on the material measure's porosity at each cumulative thickness.

The manufacturing variability between OMP and UMP defects was evaluated using the data presented in Table 4, which illustrates the degree of similarity in the characterized porosity.

Leveraging the porosity characterization data, a classification of OMP and UMP defects was developed for different slices of varying thickness (30 mm and 50 mm) in the test object. Recent literature frequently highlights the distinction between OMPs and UMPs based on their morphological features [7,8], even when only considering the two-dimensional measurands, such as diameter and form, evaluated in this study for porosity characterization [42,43]. Consequently, the proposed classification criterion for OMPs starts focusing primarily on form, specifically circularity measurements. Given that the most significant contributor to U_{MP} is the repeatability of the measurement process, the classification also incorporates the standard deviation (σ) of the repeated measurements into the criteria. High σ-values are generally associated with UMP defects and often arise due to the sharp, abrupt boundaries characteristic of these defects, where pores with higher circularity tend to exhibit higher U_{MP} values. In contrast, low σ-values typically correspond to more regular shapes, such as OMPs.

To enhance the classification process, volumetric parameters that include compactness, sphericity, mean gray value, and projected area (%) along the primary cylinder's direction are provided. While measurements were performed in 3D to support extended characterization for classification purposes, volumetric parameters were analyzed but not assigned measurement uncertainties in order to avoid inconsistencies that could arise from extrapolating a 2D uncertainty evaluation to 3D features, thus ensuring methodological coherence.

Fig. 12 illustrates the numerical results for twenty OMPs and twenty UMPs located in the OMP containing slice and UMP containing slice of the test object.

The results of the evaluated volumetric properties demonstrate varying levels of sensitivity in distinguishing between OMP and UMP defects. For example, the projected area (%) along the primary cylinder axis for OMP defects at a cumulative thickness of 30 mm is consistently larger than that of UMP defects. However, this difference becomes less pronounced at a thickness of 50 mm, where increased attenuation reduces measurement precision. In contrast, Fig. 12 illustrates that UMP defects tend to exhibit higher mean gray values compared to OMPs, likely due to the presence of unmelted powder particles within UMP defects. These particles contribute to the higher gray value, a characteristic not observed in OMP, which typically contain trapped metallic vapor and gas generated during unstable melt pool dynamics. Therefore, the mean gray value consistently proves to be the most reliable parameter for differentiating OMP from UMP defects, regardless of cumulative thickness.

Fig. 13 displays a comparative analysis of circularity, σ-values, and the relative mean gray value for each pore, where the gray value is expressed as a percentage relative to the mean gray value of the surrounding solid material in the test object. The gray value for each pore represents the average across five independent XCT scans of the test object. Both circularity and σ-values are expressed relative to the measured diameter (%) to ensure adaptability across varying pore sizes. To enhance visual clarity, projections of the data points are provided on the ZX and XY planes.

Results in the XY plane projection reveal a larger population of OMPs at lower σ (%) and circularity (%) values. Specifically, within the range of circularity below 20 % and σ-values below 4 %, 90.9 % of the pores are confirmed as OMPs, as evidenced by their exclusive presence in slices specifically designed for OMP formation. These represent the most ideal OMP-type defects, characterized by minimal form errors and enhanced consistency across measurement repetitions. However, a significant number of OMPs fell outside this region, indicating the insufficiency of this initial classification criterion alone.

The ZX plane projection clearly indicates a threshold at approximately 73.8 % relative gray value, effectively distinguishing all analyzed OMPs from UMPs. Furthermore, it highlights variations in relative mean gray values between OMPs with different cumulative thicknesses, in contrast to the absence of such distinctions for UMPs.

To further validate the reliability of the relative mean gray value as an independent factor, additional assessments were conducted on 200 pores with diameters ranging between 0.2 mm and 0.3 mm within each slice specifically designed to contain either OMP or UMP defects (see Fig. 6). XCT cross-sectional images of each pore group (OMP and UMP) at 30 mm and 50 mm cumulative thickness were included to facilitate direct comparison with the established relative gray value threshold (73.8 %). The classification outcomes based on these comparisons are displayed in Fig. 14, where a violin plot illustrates the distribution of relative gray values, confirming the categorization of each pore based on a OMP or UMP slice designation.

The violin plot shown in Fig. 14 clearly shows that the mean gray value is a key factor for the accurate classification of OMPs and UMPs. The classification accuracy is 97.99 % for OMPs and 99.50 % for UMPs in 30 mm region while, for 50 mm region, the classification accuracy is 93.43 % for OMPs and 99.50 % for UMPs.

Table 4
Comparison of diameter and circularity variability between OMP and UMP defects in the material measure and test object for assessing flaws similarity.

Flaw group	Measurand	Mean value (mm)	Max. value (mm)	min. value (mm)	Standard deviation (mm)
Material measure OMP	Diameter	0.227	0.308	0.152	0.038
	Circularity	0.059	0.102	0.040	0.018
Test object OMP	Diameter	0.265	0.333	0.179	0.042
	Circularity	0.070	0.197	0.036	0.041
Test object UMP	Diameter	0.206	0.284	0.153	0.041
	Circularity	0.070	0.126	0.033	0.028

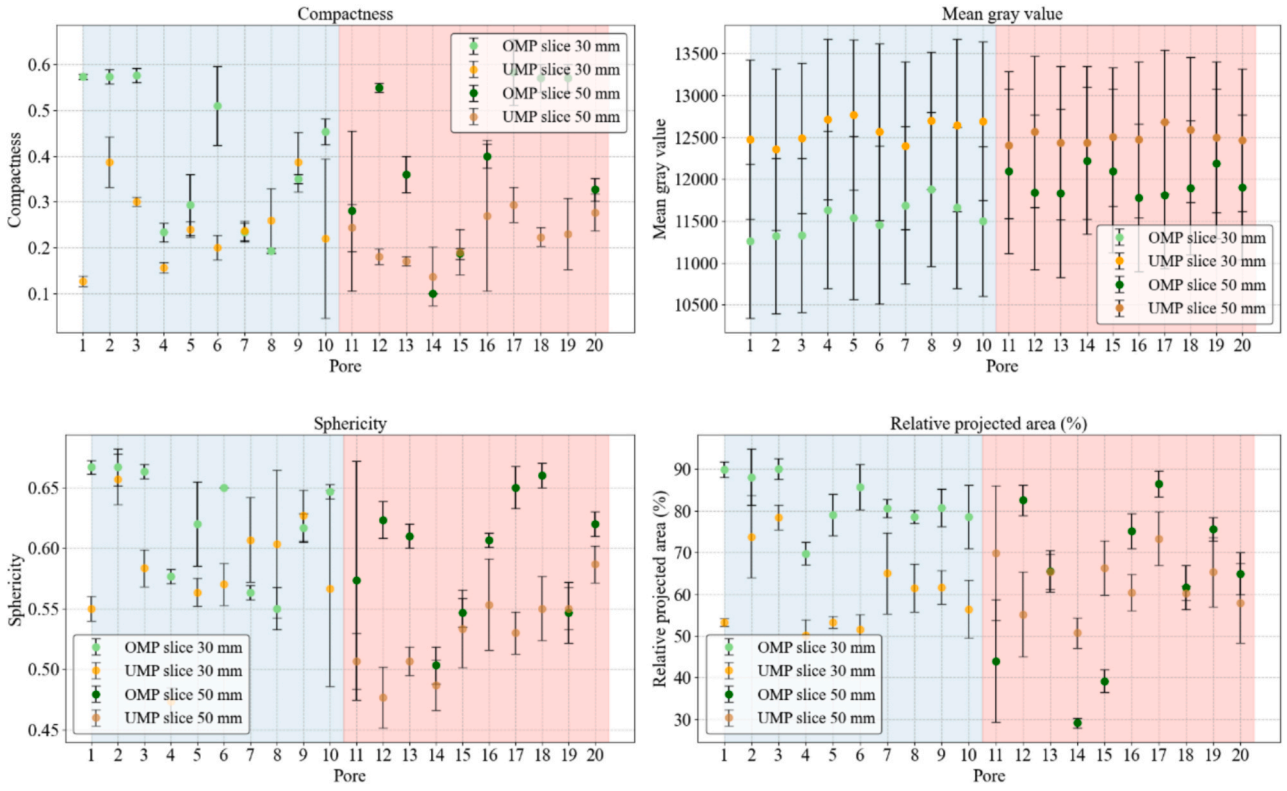

Fig. 12. Recorded properties of ten OMPs and ten UMPs extracted from 30 mm and 50 mm thick regions in the test object. The blue band represents pores in the cumulative thickness of 30 mm and the red band represents pores in the cumulative thickness of 50 mm. (For interpretation of the references to colour in this figure legend, the reader is referred to the web version of this article.)

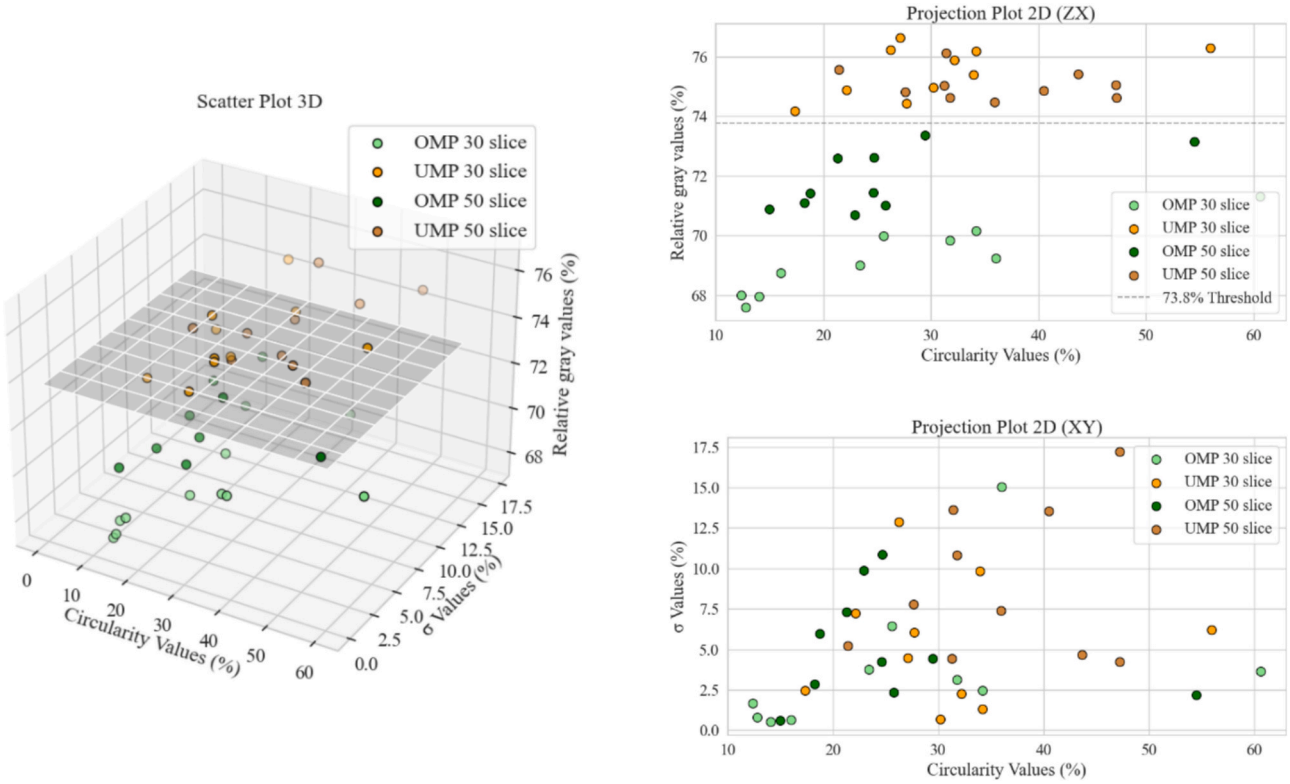

Fig. 13. 3D scatter-plot analysis of pore characteristics in the test object, illustrating relative circularity (%), relative σ-values (%), and relative mean gray value (%), with data projections on the ZX and XY planes.

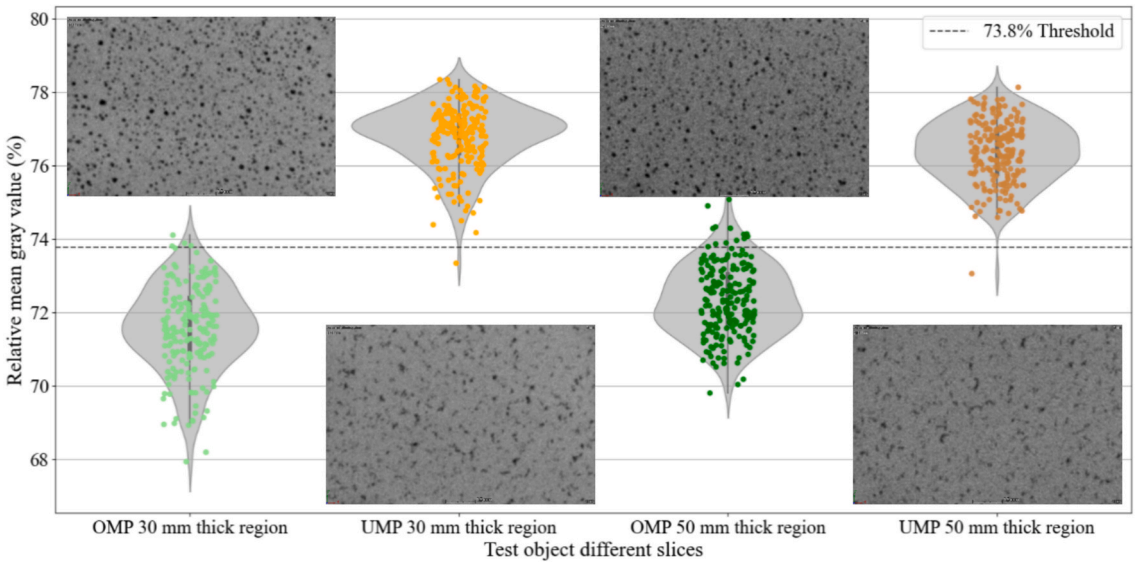

Fig. 14. Violin plot analysis of relative gray values for pores in the test object's 30 mm and 50 mm regions, designed to contain over-melted or under-melted pores. XCT cross-sectional images of each pore group are included for reference.

4. Conclusions

This study introduces a novel XCT-based methodology for metrological porosity evaluation using a modular artefact with real PBF-LB porosity, including measurement uncertainty estimation using the substitution method and defect classification based on key morphological parameters. The research findings lead to the following main conclusions:

- While calibrated artefacts are widely used for evaluating XCT measurement uncertainties, this study represents the first reported integration of artefacts specifically designed for robust real porosity measurements combined with porosity classification methods. This integrated approach enables reliable conclusions about segmented pore data characterization, measurement uncertainty, and accurate pore classification.
- The mean expanded uncertainties for both pore diameter and circularity measurements are primarily influenced by XCT process repeatability. When the pore diameter exceeds five times the voxel size used in the XCT scans, all evaluated algorithms yield consistent results, with systematic errors stabilized around the voxel size.
- VGDefX algorithm, which employs a probability-based and iterative detection approach, showed superior repeatability and remains robust despite changes in cumulative material thickness embedding the pores.
- The proposed classification criteria, leveraging volumetric mean gray value alongside pore size and measurement uncertainty, effectively distinguish over-melting from under-melting porosity with >95 % accuracy.
- The process parameters for both the material measure and the test object were intentionally adjusted to induce over-melting and under-melting defects. Although such defects would typically be minimized in optimized PBF-LB processes, the methodology proposed in this study is expected to remain valid, as it is primarily governed by XCT resolution and segmentation algorithms rather than specific manufacturing conditions. The broader applicability was further supported by a complementary high-resolution XCT evaluation at 5 μm voxel size, which confirmed consistent measurement trends for gas-entrapped pores with diameters below 0.05 mm.
- Although this methodology was demonstrated using the AlSi10Mg alloy, the systematic approach, based on a modular calibrated artefact and the substitution method, is designed to be adaptable to other materials, including high-density alloys. Provided that the outlined procedure is rigorously followed, the method remains applicable, although adjustments to scanning parameters and analysis settings may be necessary due to increased X-ray attenuation. Its implementation in high-density alloys deserves further investigation to assess potential impacts on measurement accuracy and classification reliability.

CRediT authorship contribution statement

Ibon Holgado: Writing – original draft, Methodology, Investigation, Formal analysis, Conceptualization. **Naiara Ortega:** Writing – review & editing, Validation, Supervision, Funding acquisition, Conceptualization. **José A. Yagüe-Fabra:** Writing – review & editing, Validation, Supervision, Project administration. **Soraya Plaza:** Supervision, Resources, Funding acquisition. **Herminso Villarraga-Gómez:** Writing – review & editing, Validation, Supervision, Conceptualization.

Declaration of competing interest

The authors declare that they have no known competing financial interests or personal relationships that could have appeared to influence the work reported in this paper.

Acknowledgements

This work was funded by the MCIN/AEI/10.13039/501100011033 under Grant Number PID2020-118478RB-100 and by the Basque Government's Department of Industry, Energy Transition, and Sustainability under Grant Number KK-2024/00080 (METROTEK research project). This research also received some help from Basque Government by university research groups, grant IT1573-22.

Appendix A

Table A1
Diameter and circularity XCT measurements results after 'VGDefX' algorithm surface detection on the ten selected pores of the material measure, including uncertainty contributors and expanded uncertainty U_{MP} $(k = 2)$ statements. All values not indicated are in millimeters (mm).

	Measurand	Pore N°	y_{MP}	b	u_{cal}	u_p	U_{MP}
Ø30 mm	**Diameter**	1a	0.092	−0.120	0.003	0.066	0.131
		2a	0.152	−0.092	0.003	0.031	0.062
		3a	0.202	−0.044	0.003	0.010	0.021
		4a	0.210	−0.018	0.003	0.008	0.017
		5a	0.216	−0.022	0.003	0.012	0.024
		6a	0.221	−0.021	0.003	0.018	0.037
		7a	0.249	0.013	0.003	0.012	0.024
		8a	0.251	−0.016	0.003	0.011	0.022
		9a	0.291	0.043	0.003	0.024	0.049
		10a	0.308	0.011	0.003	0.037	0.075
	Circularity	1a	0.024	0.013	0.003	0.018	0.036
		2a	0.069	0.057	0.003	0.030	0.060
		3a	0.046	0.032	0.003	0.009	0.018
		4a	0.043	0.028	0.003	0.015	0.030
		5a	0.052	0.043	0.003	0.009	0.019
		6a	0.057	0.035	0.003	0.015	0.031
		7a	0.041	0.029	0.003	0.007	0.014
		8a	0.046	0.027	0.003	0.008	0.017
		9a	0.078	0.065	0.003	0.044	0.088
		10a	0.099	0.088	0.003	0.096	0.191
Ø50 mm	**Diameter**	1b	0.176	−0.059	0.003	0.018	0.036
		2b	0.190	−0.037	0.003	0.035	0.069
		3b	0.194	−0.046	0.003	0.010	0.020
		4b	0.196	−0.008	0.003	0.007	0.015
		5b	0.201	−0.024	0.003	0.010	0.021
		6b	0.209	−0.045	0.003	0.013	0.026
		7b	0.230	−0.028	0.003	0.019	0.037
		8b	0.239	−0.032	0.003	0.024	0.048
		9b	0.256	0.026	0.003	0.008	0.017
		10b	0.266	0.036	0.003	0.009	0.018
	Circularity	1b	0.063	0.054	0.003	0.020	0.041
		2b	0.073	0.066	0.003	0.035	0.070
		3b	0.066	0.048	0.003	0.021	0.041
		4b	0.102	0.092	0.003	0.033	0.067
		5b	0.040	0.031	0.003	0.008	0.017
		6b	0.046	0.034	0.003	0.012	0.024
		7b	0.055	0.045	0.003	0.020	0.040
		8b	0.065	0.052	0.003	0.031	0.063
		9b	0.048	0.035	0.003	0.013	0.026
		10b	0.040	0.027	0.003	0.003	0.008

Table A2
Diameter and circularity XCT measurements results after ' OnlyThreshold ' algorithm surface detection on the ten selected pores of the material measure, including uncertainty contributors and expanded uncertainty U_{MP} $(k = 2)$ statements. All values not indicated are in millimeters (mm).

	Measurand	Pore N°	y_{MP}	b	u_{cal}	u_p	U_{MP}
Ø30 mm	**Diameter**	1a	0.093	−0.119	0.003	0.066	0.131
		2a	0.151	−0.093	0.003	0.032	0.064
		3a	0.202	−0.044	0.003	0.009	0.019
		4a	0.210	−0.018	0.003	0.009	0.019
		5a	0.216	−0.022	0.003	0.012	0.025
		6a	0.221	−0.021	0.003	0.018	0.037
		7a	0.250	0.014	0.003	0.011	0.023
		8a	0.251	−0.016	0.003	0.011	0.023
		9a	0.292	0.044	0.003	0.024	0.049
		10a	0.309	0.012	0.003	0.038	0.075
	Circularity	1a	0.025	0.014	0.003	0.018	0.036
		2a	0.071	0.059	0.003	0.028	0.057
		3a	0.046	0.032	0.003	0.009	0.018
		4a	0.044	0.029	0.003	0.015	0.031
		5a	0.051	0.042	0.003	0.009	0.018
		6a	0.058	0.036	0.003	0.013	0.027
		7a	0.040	0.028	0.003	0.006	0.013
		8a	0.048	0.029	0.003	0.008	0.017
		9a	0.078	0.065	0.003	0.044	0.087
		10a	0.084	0.073	0.003	0.107	0.214

(*continued on next page*)

Table A2 (*continued*)

	Measurand	Pore N°	y_{MP}	b	u_{cal}	u_p	U_{MP}
Ø50 mm	**Diameter**	1b	0.174	−0.061	0.003	0.021	0.041
		2b	0.192	−0.035	0.003	0.034	0.068
		3b	0.216	−0.024	0.003	0.067	0.134
		4b	0.202	−0.002	0.003	0.013	0.026
		5b	0.200	−0.025	0.003	0.011	0.023
		6b	0.209	−0.045	0.003	0.013	0.026
		7b	0.231	−0.027	0.003	0.019	0.038
		8b	0.248	−0.023	0.003	0.030	0.061
		9b	0.256	0.026	0.003	0.008	0.016
		10b	0.267	0.037	0.003	0.009	0.019
	Circularity	1b	0.062	0.053	0.003	0.021	0.041
		2b	0.072	0.065	0.003	0.034	0.068
		3b	0.086	0.068	0.003	0.067	0.134
		4b	0.112	0.102	0.003	0.013	0.026
		5b	0.040	0.031	0.003	0.011	0.023
		6b	0.047	0.035	0.003	0.013	0.026
		7b	0.055	0.045	0.003	0.019	0.038
		8b	0.085	0.072	0.003	0.030	0.061
		9b	0.052	0.039	0.003	0.008	0.016
		10b	0.040	0.027	0.003	0.009	0.019

Table A3
Diameter and circularity XCT measurements results after ' VGEasyPore ' algorithm surface detection on the ten selected pores of the material measure, including uncertainty contributors and expanded uncertainty U_{MP} $(k = 2)$ statements. All values not indicated are in millimeters (mm).

	Measurand	Pore N°	y_{MP}	b	u_{cal}	u_p	U_{MP}
Ø30 mm	**Diameter**	1a	0.000	−0.212	0.003	0.000	0.005
		2a	0.100	−0.144	0.003	0.035	0.071
		3a	0.163	−0.083	0.003	0.001	0.006
		4a	0.103	−0.125	0.003	0.113	0.226
		5a	0.175	−0.063	0.003	0.011	0.022
		6a	0.191	−0.051	0.003	0.020	0.039
		7a	0.222	−0.014	0.003	0.012	0.025
		8a	0.221	−0.046	0.003	0.009	0.019
		9a	0.247	−0.001	0.003	0.006	0.013
		10a	0.261	−0.036	0.003	0.011	0.022
	Circularity	1a	0.000	−0.011	0.003	0.000	0.005
		2a	0.044	0.032	0.003	0.035	0.071
		3a	0.041	0.027	0.003	0.001	0.006
		4a	0.012	−0.003	0.003	0.113	0.226
		5a	0.032	0.023	0.003	0.011	0.022
		6a	0.048	0.026	0.003	0.020	0.039
		7a	0.031	0.019	0.003	0.012	0.025
		8a	0.038	0.019	0.003	0.009	0.019
		9a	0.032	0.019	0.003	0.006	0.013
		10a	0.052	0.041	0.003	0.011	0.022
Ø50 mm	**Diameter**	1b	0.122	−0.113	0.003	0.083	0.166
		2b	0.179	−0.048	0.003	0.034	0.069
		3b	0.125	−0.115	0.003	0.086	0.171
		4b	0.149	−0.055	0.003	0.023	0.046
		5b	0.188	−0.037	0.003	0.008	0.016
		6b	0.186	−0.068	0.003	0.011	0.023
		7b	0.198	−0.060	0.003	0.021	0.042
		8b	0.182	−0.089	0.003	0.023	0.045
		9b	0.232	0.002	0.003	0.008	0.016
		10b	0.242	0.012	0.003	0.007	0.015
	Circularity	1b	0.048	0.039	0.003	0.038	0.075
		2b	0.071	0.064	0.003	0.027	0.055
		3b	0.050	0.032	0.003	0.036	0.072
		4b	0.081	0.071	0.003	0.026	0.053
		5b	0.056	0.047	0.003	0.060	0.121
		6b	0.044	0.032	0.003	0.022	0.045
		7b	0.047	0.037	0.003	0.021	0.042
		8b	0.067	0.054	0.003	0.029	0.058
		9b	0.031	0.018	0.003	0.011	0.022
		10b	0.034	0.021	0.003	0.007	0.015

Data availability

Data will be made available on request.

References

[1] C. Wei, Z. Zhang, D. Cheng, Z. Sun, M. Zhu, L. Li, An overview of laser-based multiple metallic material additive manufacturing: from macro-to micro-scales, Int. J. Extreme Manuf. 3 (2020) 012003.

[2] J. Gong, K. Wei, M. Liu, W. Song, X. Li, X. Zeng, Microstructure and mechanical properties of AlSi10Mg alloy built by laser powder bed fusion/direct energy deposition hybrid laser additive manufacturing, Addit. Manuf. 59 (2022) 103160.

[3] K.S. Stopka, A. Desrosiers, T. Nicodemus, N. Krutz, A. Andreaco, M.D. Sangid, Intentionally seeding pores in additively manufactured Alloy 718: process parameters, microstructure, defects, and fatigue, Addit. Manuf. (2023) 103450.

[4] Additive Manufacturing UK, National Strategy 2018, Additive Manufacturing UK, 2018, p. 44. (accessed October 21, 2024).

[5] J.M. Waller. Nondestructive testing of additive manufactured metal parts used in aerospace applications (Report No. JSC-E-DAA-TN49270), 2018.

[6] D. Li, X. Zhang, R. Qin, J. Xu, D. Yue, B. Chen, Influence of processing parameters on AlSi10Mg lattice structure during selective laser melting: manufacturing defects, thermal behavior and compression properties, Opt. Laser Technol. 161 (2023) 109182, https://doi.org/10.1016/j.optlastec.2023.109182.

[7] A. Poudel, M.S. Yasin, J. Ye, J. Liu, A. Vinel, S. Shao, N. Shamsaei, Feature-based volumetric defect classification in metal additive manufacturing, Nat. Commun. 13 (2022) 6369.

[8] J.C. Hastie, M.E. Kartal, L.N. Carter, M.M. Attallah, D.M. Mulvihill, Classifying shape of internal pores within AlSi10Mg alloy manufactured by laser powder bed fusion using 3D X-ray micro computed tomography: influence of processing parameters and heat treatment, Mater. Charact. 163 (2020) 110225, https://doi.org/10.1016/j.matchar.2020.110225.

[9] Additive manufacturing of metals — Non-destructive testing and evaluation — Defect detection in parts (ISO/ASTM TR 52905:2023), 2023.

[10] T. Montalbano, B.N. Briggs, J.L. Waterman, S. Nimer, C. Peitsch, J. Sopcisak, D. Trigg, S. Storck, Uncovering the coupled impact of defect morphology and microstructure on the tensile behavior of Ti-6Al-4V fabricated via laser powder bed fusion, J. Mater. Process. Technol. 294 (2021) 117113.

[11] M. Salarian, H. Asgari, M. Vlasea, Pore space characteristics and corresponding effect on tensile properties of Inconel 625 fabricated via laser powder bed fusion, Mater. Sci. Eng. A 769 (2020) 138525.

[12] W.H. Kan, M. Gao, X. Zhang, E. Liang, N.S.L. Chiu, C.V.S. Lim, A. Huang, The influence of porosity on Ti-6Al-4V parts fabricated by laser powder bed fusion in the pursuit of process efficiency, Int. J. Adv. Manuf. Technol. 119 (2022) 5417–5438, https://doi.org/10.1007/s00170-021-08374-8.

[13] I. Maskery, N.T. Aboulkhair, M.R. Corfield, C. Tuck, A.T. Clare, R.K. Leach, R. D. Wildman, I.A. Ashcroft, R.J.M. Hague, Quantification and characterisation of porosity in selectively laser melted Al–Si10–Mg using X-ray computed tomography, Mater. Charact. 111 (2016) 193–204, https://doi.org/10.1016/j.matchar.2015.12.001.

[14] J. Tkac, T. Toth, V. Molnar, M. Dovica, G. Fedorko, Observation of porous Structure's deformation wear after axial loading with the use of Industrial computed tomography (CT), Measurement 200 (2022) 111631, https://doi.org/10.1016/j.measurement.2022.111631.

[15] M. Jakubowicz, P. Mietliński, J. Królczyk, G. Budzik, P. Niesłony, A. Trych-Wildner, N. Wojciechowska, G. Królczyk, M. Wieczorowski, J. Staśkiewicz, T. Bartkowiak, Parametric Evaluation Samples Made by SLM Technology Measured Using Micro-Computed Tomography, in: M. Diering, M. Wieczorowski, M. Harugade (Eds.), Adv. Manuf. IV, Springer Nature Switzerland, Cham, 2024: pp. 83–95. doi: 10.1007/978-3-031-56467-3_7.

[16] P.J. Withers, C. Bouman, S. Carmignato, V. Cnudde, D. Grimaldi, C.K. Hagen, E. Maire, M. Manley, A. Du Plessis, S.R. Stock, X-ray computed tomography, Nat. Rev. Methods Primer 1 (2021) 1–21.

[17] H. Villarraga-Gómez, J.D. Thousand, S.T. Smith, Empirical approaches to uncertainty analysis of X-ray computed tomography measurements: A review with examples, Precision Engineering 64 (2020) 249–268.

[18] W. Dewulf, H. Bosse, S. Carmignato, R. Leach, Advances in the metrological traceability and performance of X-ray computed tomography, CIRP Ann. 71 (2022) 693–716.

[19] B. Muralikrishnan, M. Shilling, S. Phillips, W. Ren, V. Lee, F. Kim, X-ray computed tomography instrument performance evaluation, part I: sensitivity to detector geometry errors, J. Res. Natl. Inst. Stand. Technol. 124 (2019) 1–16, https://doi.org/10.6028/jres.124.014.

[20] J.J. Lifton, T. Liu, Evaluation of the standard measurement uncertainty due to the ISO50 surface determination method for dimensional computed tomography, Precis. Eng. 61 (2020) 82–92, https://doi.org/10.1016/j.precisioneng.2019.10.004.

[21] Á. Rodríguez-Sánchez, A. Thompson, L. Körner, N. Brierley, R. Leach, Review of the influence of noise in X-ray computed tomography measurement uncertainty, Precis. Eng. 66 (2020) 382–391, https://doi.org/10.1016/j.precisioneng.2020.08.004.

[22] Geometrical product specifications (GPS). Coordinate measuring machines (CMM). Technique for determining the uncertainty of measurement. Part 4: Evaluating task-specific measurement uncertainty using simulation (ISO/TS 15530-4:2008), 2008.

[23] B.A. Bircher, S. Wyss, D. Gage, A. Küng, C. Körner, F. Meli, High-resolution x-ray computed tomography for additive manufacturing: towards traceable porosity defect measurements using digital twins, in: Jt. Spec. Interest Group Meet. Euspen ASPE Adv. Precis. Addit. Manuf. Inspire AG, 2021.

[24] W. Liu, X. Chen, W. Zeng, W. Sun, D. Gorman, A. Wilson, Q. Qi, P. Scott, X. Jiang, S. Lou, Comparison of X-ray computed tomography and coordinate-measuring system dimensional measurement for additive manufacturing parts using physical and simulation methods, Measurement 229 (2024) 114414, https://doi.org/10.1016/j.measurement.2024.114414.

[25] M. Ferrucci, E. Ametova, Charting the course towards dimensional measurement traceability by x-ray computed tomography, Meas. Sci. Technol. 32 (2021) 092001.

[26] F. Zanini, S. Carmignato, E. Savio, Two different experimental approaches for the uncertainty determination of X-ray computed tomography dimensional measurements on lattice structures, CIRP J. Manuf. Sci. Technol. 47 (2023) 205–214, https://doi.org/10.1016/j.cirpj.2023.10.004.

[27] Computed tomography in dimensional measurement. VDI/VDE 2630 Part 2.1: Determination of the uncertainty of measurement and the test process suitability of coordinate measurement systems with CT sensors, 2015.

[28] Geometrical product specifications (GPS). Coordinate measuring machines (CMM). Technique for determining the uncertainty of measurement. Part 3: Use of calibrated workpieces or measurement standards (ISO 15530–3:2011), 2011.

[29] P. Hermanek, S. Carmignato, Porosity measurements by X-ray computed tomography: accuracy evaluation using a calibrated object, Precis. Eng. 49 (2017) 377–387.

[30] J. Lesseur, B. Tranchand, T. Mancier, A. Montauzier, C. Larignon, S. Perusin, On the use of X-ray microtomography to control artificial defect geometries produced by metal additive manufacturing, Nondestruct. Test. Eval. 37 (2022) 611–630.

[31] A. Staude, M. Bartscher, K. Ehrig, J. Goebbels, M. Koch, U. Neuschaefer-Rube, J. Nötel, Quantification of the capability of micro-CT to detect defects in castings using a new test piece and a voxel-based comparison method, NDT E Int. 44 (2011) 531–536, https://doi.org/10.1016/j.ndteint.2011.05.006.

[32] Y. Chahid, C. Packer, A. Tawfik, J. Keen, N. Brewster, M. Beardsley, K. Morris, P. Bills, L. Blunt, C. Atkins, S. Tammas-Williams, Development of a modular system to provide confidence in porosity analysis of additively manufactured components using x-ray computed tomography, Meas. Sci. Technol. 35 (2024) 045023, https://doi.org/10.1088/1361-6501/ad1670.

[33] J. Lifton, T. Liu, An adaptive thresholding algorithm for porosity measurement of additively manufactured metal test samples via X-ray computed tomography, Addit. Manuf. 39 (2021) 101899.

[34] Q. Luo, L. Yin, T.W. Simpson, A.M. Beese, Effect of processing parameters on pore structures, grain features, and mechanical properties in Ti-6Al-4V by laser powder bed fusion, Addit. Manuf. 56 (2022) 102915, https://doi.org/10.1016/j.addma.2022.102915.

[35] J. Sun, J. Su, C. Ma, R. Göstl, A. Herrmann, K. Liu, H. Zhang, Fabrication and mechanical properties of engineered protein-based adhesives and fibers, Adv. Mater. 32 (2020) 1906360.

[36] European Cooperation for Accreditation, Evaluation of the Uncertainty of Measurement in Calibration (EA-4/02 M:2022), 2022.

[37] F. Zanini, M. Sorgato, E. Savio, S. Carmignato, Dimensional verification of metal additively manufactured lattice structures by X-ray computed tomography: use of a newly developed calibrated artefact to achieve metrological traceability, Addit. Manuf. 47 (2021) 102229.

[38] M. Praniewicz, J.C. Fox, C. Saldana, Toward traceable XCT measurement of AM lattice structures: uncertainty in calibrated reference object measurement, Precis. Eng. 77 (2022) 194–204.

[39] A. Salah, L. Blunt, P. Bills, A contribution to the debate on measurement uncertainty when using X-ray computing tomography, E-J. Nondestruct. Test. 28 (2023), https://doi.org/10.58286/27758.

[40] K.M. Guan, M. Nazarova, B. Guo, H. Tchelepi, A.R. Kovscek, P. Creux, Effects of image resolution on sandstone porosity and permeability as obtained from X-ray microscopy, Transp. Porous Media 127 (2019) 233–245, https://doi.org/10.1007/s11242-018-1189-9.

[41] B. Jolley, C. Knott, D. Sparkman, M. Uchic, Comparative analysis of internal porosity in AM Ti64 using X-ray computed tomography and mechanical polishing serial sectioning, IEEE Open J. Instrum. Meas. 3 (2024) 1–11, https://doi.org/10.1109/OJIM.2024.3477569.

[42] M. Mirz, S. Herzog, C. Broeckmann, A. Kaletsch, Influence of the L-PBF process atmosphere on the microstructure and tensile properties of AISI 318LN duplex stainless steel, J. Manuf. Mater. Process. 6 (2022) 32, https://doi.org/10.3390/jmmp6020032.

[43] A. du Plessis, S.G. le Roux, A. Guelpa, Comparison of medical and industrial X-ray computed tomography for non-destructive testing, Case Stud. Nondestruct. Test. Eval. 6 (2016) 17–25, https://doi.org/10.1016/j.csndt.2016.07.001.